Surface layer formation in the earliest stages of corrosion of steel in CO_2-saturated brine at 80°C, studied by *in situ* synchrotron X-ray methods

Bridget Ingham,[1] William Holmes-Hewett,[1] Monika Ko,[2a] Nigel M. Kirby,[3] Mobbassar Hassan Sk,[4b] Aboubakr M. Abdullah,[4] Nicholas J. Laycock[5] and David E. Williams[6,*]

1 Callaghan Innovation, P.O. Box 31310, Lower Hutt 5040, New Zealand

2 Quest Integrity Group, P.O. Box 38096, Lower Hutt 5045, New Zealand

3 Australian Synchrotron, 800 Blackburn Road, Clayton, VIC 3168, Australia

4 Center for Advanced Materials, Qatar University, Doha 2713, Qatar

5 Qatar Shell Research and Technology Centre, P.O. Box 3747, Doha, Qatar

6 School of Chemical Sciences and MacDiarmid Institute for Advanced Materials and Nanotechnology, University of Auckland, Private Bag 92019, Auckland 1142, New Zealand

Abstract

Grazing-incidence small-angle X-ray scattering (GISAXS) from polycrystalline steel shows features associated with the underlying microstructure, and, in the initial stages of corrosion, with the development of very small-scale surface roughness, on the nanometer height scale. A 1Cr0.25Mo pipeline steel in hot, CO_2-saturated brine develops the very small-scale surface roughness significantly faster than a simple carbon steel, although the overall dissolution current density for the two steels is almost the same. We speculate that

[a] Present address: Qatar Shell Research and Technology Centre, P.O. Box 3747, Doha, Qatar
[b] Present address: BP Institute and Department of Chemistry, Cambridge University, Lensfield Road, Cambridge, United Kingdom, CB2 1EW

it is due to the presence of a layer comprising 'blobs' of amorphous $FeCO_3$, which grow to spread over the surface and eventually cover it, because it is significantly larger in height scale than the roughness developed during the initial stages of anodic dissolution in acidified NaCl solution, where no surface film is expected. The greater roughness on the 1Cr0.25Mo steel can be interpreted as due to small pre-crystalline nuclei, that form at much lower supersaturation, and grow faster, than on mild steel. Grazing-incidence X-ray diffraction studies show at later stages the apparent preferential dissolution of smaller crystallites of iron, with spatial size scale 0.1 – 1 μm. This develops significantly more slowly on the 1Cr0.25Mo than on the simple carbon steel.

Keywords: small-angle X-ray scattering, anodic film, carbon dioxide, corrosion, iron carbonate

Introduction

The formation of crystalline layers of siderite is important for the diminution of corrosion rate of carbon steel in hot, CO_2-saturated brine – a phenomenon of some importance for management of corrosion of oil and gas production pipelines (1). The corrosion reaction is complex (2): iron dissolves as a carbonato complex of some sort (3), to form a colloidal product assumed to be amorphous iron carbonate (4); the growth of siderite requires a significant critical supersaturation (4-6); and the supersaturation is controlled by the transport of dissolved CO_2, the dissolution rate of iron and the precipitation rate of the colloidal iron carbonate (2). Dissolution of iron is presumed to occur through a surface layer of amorphous iron carbonate (2). The presence of Cr and of Mo either in the steel or in the solution has a significant effect on the critical supersaturation and growth of siderite and on the precipitation kinetics of the colloidal iron carbonate (4, 7, 8). Within this framework,

understanding the kinetics of formation and growth of the amorphous carbonate layer that is presumed to control the dissolution rate comes into focus. The presence of this film is deduced from the effect on the current (3, 9). A completely passivating film, deduced to be a 2-layer film comprising hydrous Fe(II,III) oxides, can be formed at room temperature, pH 9.2 and has been studied ellipsometrically (10). However, this is unlikely to be a model for the dissolving layer formed at high temperature and lower pH. In earlier work, we presented a grazing-incidence small-angle X-ray scattering (GISAXS) study of the first stages of siderite crystallisation during CO_2 corrosion of carbon steel (4). We interpreted the results as indicating three phases in the development of the surface layer: the initial formation of a discontinuous layer comprising 'blobs' of amorphous $FeCO_3$, which subsequently grow to spread over the surface and eventually cover it; then the appearance of a new set of scatterers with lateral size scale ≈ 20 nm, interpreted as pre-nucleation clusters; then finally the nucleation and growth of crystals, which is signalled by the appearance of a crystalline diffraction pattern. The effect of the presence of trace Cr^{3+} in the solution could be interpreted as a significant acceleration and overlapping of all three stages. The present work reports extension of the GISAXS study to cover different alloys and develops more detail concerning the initial stages of the corrosion reaction.

Experimental

GISAXS experiments were performed on the SAXS/WAXS beamline at the Australian Synchrotron (11). Steel rods 2 mm in diameter were coated in epoxy and the top surfaces polished using 1 micron diamond paste to an optically smooth finish. Two types of steel were studied. The AISI 1006 simple carbon steel (mild steel) sample had an equiaxed ferritic/pearlitic microstructure in both transverse and longitudinal cross section to the

drawing direction. It was relatively free of inclusions and had a grain size of ~10 µm, typical of hot formed low carbon steel. The as-received API 5CT L80 1Cr0.25Mo pipeline steel (supplied by Tenaris) had a quenched and tempered martensitic microstructure, with high yield strength and mechanical properties appropriate for use for well applications. Micrographs are given in the Supporting Information (SI): figure S1. Each rod was mounted in an electrochemical cell as used previously for *in situ* synchrotron X-ray diffraction experiments (6, 12). It featured a solution reservoir, that fitted snugly into a heating jacket, and which tapered to a narrow slot just above the electrode mounted in the base. The solution path length at the electrode was approximately 2.5 mm. X-rays of wavelength 0.8265 Å (15 keV) struck the rod at grazing incidence; the exact incidence angle was unknown, but was determined from the initial position of the diffuse reflected beam to be less than 0.5°. The synchrotron beam was 0.1 mm wide and spilled over the entire length of the sample. Scattered X-rays were detected using a Pilatus 1 M detector located 6.73 m from the sample. This gave a horizontal angular range of $-0.63 < \theta_f < 0.80$ degrees (q range of -0.084 Å$^{-1} < q_{xy} < 0.107$ Å^{-1}) and vertical angular range of $-0.39 < \alpha_f < 1.14$ degrees (q-range of -0.051 Å$^{-1} < q_z < 0.152$ Å^{-1}). The exposure time for each image was 4 s. Thermal heating by the synchrotron beam is negligible; although the flux is high, the energy bandwidth and therefore the total power of the beam is low (for a beam of similar flux and energy focussed into an area a factor of 10^7 smaller a temperature rise of 8 K has been calculated (13)) . A more significant problem is the formation of radical species and hydrogen bubbles due to radiation damage. In preliminary work with images continuously recorded, we noted using the wide-angle detector, that a diffraction pattern of chukanovite ($Fe_2(OH)_2CO_3$) appeared much more rapidly than expected (an explanation is the effect of a local pH change that could be caused by radiolysis). When the radiation dose was reduced

by attenuating the flux and reducing the image acquisition frequency then the formation of crystalline products occurred on timescales commensurate with those observed in experiments in the absence of X-rays (2). Thus, in the present work, the X-ray flux was reduced to 25% of the full beam using attenuators , images were recorded continuously for 1 minute at the open-circuit potential, the electrode potential was stepped to the desired value, images were recorded continuously for 2 minutes, then reduced in frequency to one image every minute. The electrochemical tests were performed using a 0.5 M NaCl solution that was heated to 80°C and saturated with CO_2 by continuously bubbling CO_2 gas for at least 1 hr, with pH adjusted by adding 2 M NaOH (20 mL per litre NaCl solution). This gave a calculated pH of 6.8 at 80°C (6.3 at room temperature). The hot solution was transferred to the cell and CO_2 was bubbled continuously throughout the experiment. The cell was aligned in the X-ray beam whilst the temperature stabilised. The open circuit potential was in the range -0.71 to-0.73VAg|AgCl, 3 M KCl. Data processing was performed using software developed in-house. The raw data images were rotated about the beam centre so that the specular reflection was aligned in the vertical direction. Cuts at constant q_{xy} and q_z could then be obtained for each image (although in this manuscript we focus mainly on the cuts at constant q_{xy}). The same cell and procedure was used for grazing-incidence X-ray diffraction measurements, performed separately on the Powder Diffraction (PD) beamline of the Australian Synchrotron.

Results and Discussion

GISAXS results from a typical *in situ* experiment, where the sample was corroded under potentiostatic control, are shown in Figures 1-2. Additional images are given in the SI.

Initially, several features were observed: (a) a strong specular streak, which consists of a peak with a series of additional oscillations in q_z, (b) broad diffuse scattering around the specular reflection, and (c) isotropic scattering at low q near the beam centre. As the experiment progressed, the specular peak and its oscillations moved to lower q_z, as did the diffuse scattering. The amplitude of the oscillations decreased with time. At longer times the isotropic scattering increased and eventually dominated the signal.

The shift in the position of both the specular peak and the oscillations to lower q_z, and the damping of the oscillations over time, were particularly clear for measurements conducted at the open-circuit potential (Figure 2). The time-scale over which the changes occurred was significantly shorter for samples that were anodically polarised: Figure 3. The oscillations were observed both in the absence of the solution (figure S2) and in the presence of the solution when the steel had been cathodically polarised to remove any air-formed surface film possibly present (figure S3). The timescales for these changes differed significantly for the mild steel compared to the 1Cr0.25Mo steel (Figure S4)

For a sample corroded anodically in 0.03 M HCl + 0.5 M NaCl electrolyte at room temperature, a similar but much smaller shift in position of the specular reflection was observed (Figure S5). The oscillations were also present, but less marked, and their damping with time was also less marked. In this medium, no surface film was expected based on electrochemical measurements (14); literature X-ray photoelectron spectroscopy results indicate any film present to have a thickness less than 2-5 nm (15). Thus the differences in behaviour between this sample and the one corroded in the CO_2 solution are likely due to the formation of a surface film. However, as we will show, this process involves multiple

135 factors that all contribute to changes in the surface roughness and hence the scattering
136 features observed.

137 The features we are most interested in are the specular and diffuse scattering. The isotropic
138 scattering arises from the solution and the cell windows, plus particles suspended in
139 solution and/or that adhere to the windows of the cell; the formation of these particles
140 explains why the signal at low q increases at later times. Features commonly observed in
141 GISAXS patterns include specular reflections, Yoneda peaks, Kiessig fringes and off-axis
142 scattering. Specular scattering occurs when the reflection condition is satisfied, i.e. when
143 the exit angle α_f is equal to the incident angle α_i. In most GISAXS studies the incident angle is
144 chosen to be close to or below the critical angle α_c for total external reflection of the X-rays,
145 so that substrate effects are minimised. Yoneda peaks (or 'wings') are observed at an exit
146 angle α_f equal to the critical angle α_c. At this position there is an intensity enhancement due
147 to the propagation of the evanescent wave. Where there is a thin film on top of a substrate
148 and the different materials have different indices of refraction for X-rays (and therefore
149 different critical angles), it is possible to observe multiple Yoneda peaks (16). Kiessig fringes
150 are oscillations arising from interference from the two interfaces of a thin film (i.e.
151 substrate-film and film-air). They may be observed either on the specular features (i.e.
152 q_{xy}=0) or form factor scattering features (17, 18) . Finally, off-axis scattering arises from the
153 presence of scattering objects on or embedded in the surface, including pits. This can
154 comprise both form factor scattering, from the size and shape of the objects, and structure
155 factor scattering, from their spacing and regularity (19-21).

156 In our scattering data, the specular peak is much broader than expected for a typical GISAXS
157 pattern. This is due to the fact that the electrodes were not perfectly flat, but, as a result of

158 the polishing method, they were slightly rounded. This means that the angle of incidence
159 was not well-defined, thus broadening the specular scattering in both the vertical and
160 horizontal directions. Another contributing factor to the broadness of the specular peak and
161 the presence of diffuse scatter is the fact that although the electrode was polished to an
162 optically smooth finish, it was not *atomically* smooth. To test whether random surface
163 roughness alone could account for the diffuse scatter observed, we used the method of
164 Ward (22), who gave simple equations in angular space for calculating the diffuse reflection
165 of light. The detail is given in the SI. The calculation reproduced the observed initial diffuse
166 scattering, a spot that is broader in the vertical direction than the horizontal, with small
167 values for the RMS roughness (SI). The broadening of the specular reflection also means it is
168 unlikely that we would be able to observe any Yoneda features in our scattering data, as
169 these will also be broadened and/or obscured.

170 The presence of oscillations along the specular direction is reminiscent of Kiessig fringes
171 arising from interference by a thin film, however, they were also observed when no surface
172 film was present: (a) the as-prepared electrodes with no solution present (Fig. S2); (b) at the
173 start of an experiment, before any corrosion product nuclei would have been formed on the
174 surface (Figure S3); and (c) while the steel electrode was negatively polarised (even to the
175 extent of significant hydrogen evolution) to remove any air-formed surface film that might
176 possibly be present (Fig. S3). Given that for a material such as our steel, having a complex
177 microstructure, some elements of which have different X-ray scattering characteristics, a
178 plausible explanation is that the oscillations are due to particles of Fe_3C emerging at the
179 surface, i.e. at the grain boundaries, the size-scale of the steel microstructure being
180 commensurate with the scale probed by the GISAXS experiment. The calculated scattering
181 from such second-phase particles (Figure S6) exhibits form factor oscillations along the

specular peak that are similar to the experimental data when superimposed on the broad specular scattering peak. The detail of the calculation is given in the SI, using X-ray scattering parameters appropriate for Fe and Fe_3C. Thus, the oscillations cannot be taken as evidence for a film on the electrode surface.

We therefore attribute the scattering features as follows: The broad specular peak and the diffuse scattering arise from the surface roundedness and roughness, while the oscillations arise from the steel microstructure (the distribution of Fe_3C). However, neither of these explanations can account for the movement of the specular peak (and the oscillations) to lower angles as the experiment progressed. In fact, the only explanation for the movement of the specular peak is for the incidence angle to change. Another observation to note is the damping of the oscillations as the experiment progressed.

In the initial stages of the experiment, the metal dissolves, assumed through the formation of a thin, amorphous surface film (2). The surface roughness would increase. Two factors could contribute to an increase of surface roughness: the formation of a surface deposit that is itself rough; and smaller metal crystals dissolving in preference to larger ones, perhaps as a consequence of the dissolution rate constant varying with position away from a grain boundary or inclusion, or different metal crystal faces dissolving at different rates (23). In addition, the Fe_3C particles do not dissolve. As a result, the corroded microstructure may have sufficiently deep features to cause a change in the average angle at which the incident beam strikes the surface. If these surface features were much larger than the X-ray wavelength, then a classical approach can be used to calculate the scattering, based on geometry and the law of reflection We simply modelled the developing surface roughness as a sine function, superimposed on a second sine function to model the slight rounding of

205 the surface due to the polishing, and considering the initial macroscopic roughness just as
206 something which would impose a diffuse scattering on top of the calculated effect. The
207 detail is in the SI. The calculated effect of a sinusoidal surface roughening, now on the nm
208 scale, is to move the peak position to lower angles. This occurs both when the number of
209 periods and when the amplitude increase. Thus surface roughening can qualitatively explain
210 the experimentally observed movement of the peak to lower q_z as the experiment
211 progressed. Given the sine wave approximation for the surface profile, the change in
212 reflection angle from the start of the experiment can be related to the change in average
213 gradient of the surface with respect to the surface plane, which is the chord of the sine
214 function, $\Delta g = \Delta(2h/\Lambda)$, where *h* denotes the amplitude and Λ the wavelength of the
215 model sine function. Figure 4 compares the results for the two steels, showing also the
216 variation of the current with time, and the variation in the fractal dimension derived from
217 the development of 'spottiness' in the diffraction ring for Fe, measured in a separate
218 experiment (24). The fractal dimension is related to the distribution of crystallite sizes. An
219 increase in the fractal dimension corresponds to an increase in the average crystallite size
220 probed by the X-ray beam. In our earlier work, this was attributed to preferential dissolution
221 of smaller Fe grains (6, 23, 24). Figure 5a shows the variation of Δg with time, comparing the
222 two different steels under anodic polarisation and also comparing variation for the mild
223 steel at the open circuit condition with that under anodic polarisation. Figure 5b compares
224 the variation of Δg for the two steels under CO_2 corrosion with the mild steel under anodic
225 corrosion in acidic NaCl solution (scattering data in Figure S5).

226 The results show a semi-logarithmic variation of the surface roughness measure, Δg, over
227 the whole time when the current was constant, before a detectable crystalline film

nucleated on the surface. The consistency of electrochemical results taken on the two different synchrotron visits is notable (current densities shown in Figure 4). The semilogarithmic time variation illustrates the very rapid development of very small size-scale features, which then slows with time. .The variation in reflection angle in the GISAXS experiment reveals the development of surface roughness on the nm scale. That deduction is based on the assumption of a size scale for Λ. If we follow through an assumption that the small-scale roughness is caused by the growth of a surface film, then it is reasonable to assume that the growth might be modulated by crystallite grain boundaries emerging at the surface – because growth or dissolution can be different on different crystal faces or at grain boundaries (25-29)- or by the emergence of Fe_3C at the surface. If Λ is taken as the average crystallite size or distance between Fe_3C plates revealed in the micrographs of the etched surfaces (~10 μm) then *h* is of order 10nm, since Δg is of order 10^{-3}. However, the result can also be explained with much smaller scales of Λ and *h*: the simulations given in the SI show that the observed variation of Δg could also be obtained with *h* of scale 1 nm or less, that is with Λ of scale 0.1 – 1 μm. The growth of anodic oxides results in a roughness developing on the nm scale, even on single-crystal substrates (30) so these size scales for the developing surface roughness are not unexpected for formation of an anodic layer. Figure 5a shows that the time scale for the development of surface roughness for the mild steel decreases with increasing anodic polarisation, as would be expected for a surface roughness change driven by an anodic reaction.

The comparison between the average surface gradient developed under CO_2 corrosion and that developed under anodic dissolution in acidic solution (Figure 5b) in part discriminates between roughness developed as a consequence of anodic dissolution (e.g. different

dissolution rates of different size crystallites, or different dissolution rates close to grain boundaries or inclusions) from roughness developed as a consequence of surface film growth. The acid dissolution was performed under galvanostatic conditions, at first at a low current density, to avoid any precipitation of $FeCl_2$ and then at a similar total dissolution rate to that found in the CO_2 experiments, and the comparison is made in terms of total charge passed, again to compare surface gradient developed with the same amount of material dissolved. The measured changes were much smaller, implying that the initial development of surface roughness in the CO_2 corrosion experiment (on a nm scale) can be attributed to the development of a thin but rough surface layer.

We have extensively discussed the nucleation and growth of the crystalline siderite, signalled by the current peak for the mild steel (2, 4, 6-8, 12, 24, 31-33). On the 1Cr0.25Mo pipeline steel the current peak is absent and we have interpreted this in terms of the effect of Cr and Mo decreasing the critical supersaturation for formation of crystalline siderite (4, 7, 8). Figures 4 and 5 show that, although the total current density for these two steels was very similar, the time scale for development of surface roughness of the 1Cr0.25Mo pipeline steel was shorter than that for the mild steel, at the same electrode potential, though the slope of the semilogarithmic time dependence is similar. It would appear that the very smallest roughness scales appear more rapidly on the 1Cr0.25Mo pipeline steel than on the mild steel. One hypothesis, which we have previously advanced, is that these smallest roughness scales reflect the nucleation and initial growth of amorphous ferrous carbonate, in the form of nm-scale lumps (4), similar to models advanced for the initial stages of anodic film formation by vertical growth and lateral spreading from nucleation centres (34). The more rapid appearance of roughness on this size scale on the 1Cr0.25Mo pipeline steel than on the mild steel is consistent with the hypothesis that Cr and Mo in the steel accelerate the

precipitation of amorphous iron carbonate and increase the growth rate, eventually leading to microcrystalline protective layers.

The damping of the oscillations in the scattering pattern in the very first stages of dissolution, as dissolution progresses, implies that the microstructural contrast between Fe_3C and Fe in the substrate steel that gives rise to these oscillations becomes obscured. The simplest explanation is that the X-rays reflected from the substrate become attenuated in passing through a surface layer. The surface layer could be simply due to the physical roughness – a mixture of Fe and water - or could be the amorphous $FeCO_3$ that is assumed to be present, if this were of sufficient thickness. At this X-ray wavelength, the attenuation length of either $FeCO_3$ or of a layer that is 50 vol% Fe with water is of order 100 μm. The angle of incidence of X-rays on the surface is in the range α_i = 0.1 – 0.5°. Thus the path length of X-rays through a surface layer of thickness *s* would be $2s / \sin\alpha_i$. Given an attenuation length of 100 μm, damping of the reflection oscillations would imply $s \sim 0.1 –$ 0.5 μm. This is larger though still consistent with the presumed size scale for development of the surface roughness, discussed above, within the limitations of the approximations used to interpret the data.

Whereas GISAXS reveals the variation in morphological roughness, the variation in fractal dimension of the Fe diffraction peak revealed by the grazing-incidence diffraction experiment, that develops later in the course of the experiment, was interpreted in terms of a change in crystallite size distribution intersecting the X-ray beam: that is , a corrosion-induced surface roughening by removal of material from the surface, which is distinct from the model of surface film growth advanced for the interpretation of the GISAXS data. Interpretation of the variation of fractal dimension required a crystallite size scale of

dissolving material in the range 0.1 to 10 µm, of relative amount 10^4: 10^3: 1 for 0.1, 1 and 10 µm features respectively at the start changing to 10^3: 10^2: 1 at the end (23). The spatial heterogeneity of dissolution rate, on size scales smaller than are revealed in electron micrograph images of the etched microstructure, is remarkable. The semilogarithmic variation with time can be interpreted as reflecting the frequency distribution of the metal crystallites of different size scale, with the progressive dissolution of the smaller crystallites leaving the surface roughness dominated by the larger ones. This change in crystallite size distribution at the surface (which is presumed to relate to the morphological roughness) develops significantly more slowly on the 1Cr0.25Mo steel than on the mild steel, because siderite crystals nucleate and grow more rapidly, causing the current to fall as the dissolution becomes blocked by the crystalline layer, as previously shown.

This work has illustrated the difficulties and subtleties of interpretation that appear when GISAXS is applied to *in situ* electrochemical studies of polycrystalline materials. It has also illustrated that appropriate comparison can reveal significant detail concerning the development of surface layers on nm thickness scales, even when the system is not ideal. Previously presented interpretations of the effects of microalloying on the formation of surface layers during CO_2 corrosion of steel in hot brine have been strengthened. The method has some application in evaluating the effects of different microalloying additions to the steel, particularly in following the initial slow evolution of the surface at the corrosion potential, before the nucleation and growth of the protective crystalline siderite.

Acknowledgement

This work was supported by: New Zealand Ministry of Business, Innovation and Employment, contract CO8X1003; the New Zealand Synchrotron Group Ltd; and Qatar National Research Fund (QNRF, a member of the Qatar Foundation) through National Priority Research Program (NPRP) Grant, Project No. NPRP 7-146-2-072. Although QNRF sponsored this project, it neither endorses nor rejects the findings of this research. DEW acknowledges support from the MacDiarmid Institute for Advanced Materials and Nanotechnology, NZ. Thanks also to Nick Birbilis (Monash University) for his generous advice and loan of equipment, to Erich Kisi (University of Newcastle, Australia) for the use of the VHR detector and to Bijan Kermani and Tenaris Ltd for the gift of pipeline steel. This research was undertaken on the Small Angle X-Ray Scattering and Powder Diffraction beam lines at the Australian Synchrotron, Victoria, Australia. The views expressed herein are those of the authors and are not necessarily those of the owner or operator of the Australian Synchrotron.

Competing Interests: The authors declare no competing interests

References

1. M. Kermani and A. Morshed, *Corrosion*, **59**, 659 (2003).
2. M. H. Sk, A. M. Abdullah, M. Ko, B. Ingham, N. Laycock, R. Arul and D. E. Williams, *Corrosion Science*, **126**, 26 (2017).
3. D. Davies and G. Burstein, *Corrosion*, **36**, 416 (1980).
4. B. Ingham, M. Ko, N. Laycock, N. M. Kirby and D. E. Williams, *Faraday Discussions*, **180**, 171 (2015).
5. D. Burkle, R. De Motte, W. Taleb, A. Kleppe, T. Comyn, S. M. Vargas, A. Neville and R. Barker, *Electrochimica Acta*, **255**, 127 (2017).
6. B. Ingham, M. Ko, G. Kear, P. Kappen, N. Laycock, J. A. Kimpton and D. E. Williams, *Corrosion Science*, **52**, 3052 (2010).
7. M. H. Sk, A. M. Abdullah, J. Qi, M. Ko, B. Ingham, N. Laycock, M. P. Ryan and D. E. Williams, *Journal of the Electrochemical Society*, **165**, C278 (2018).
8. M. Ko, B. Ingham, N. Laycock and D. E. Williams, *Corrosion Science*, **80**, 237 (2014).
9. B. R. Linter and G. T. Burstein, *Corrosion Science*, **41**, 117 (1999).

10. P. Southworth, A. Hamnett, A. M. Riley and J. M. Sykes, *Corrosion Science*, **28**, 1139 (1988).
11. N. M. Kirby, S. T. Mudie, A. M. Hawley, D. J. Cookson, H. D. T. Mertens, N. Cowieson and V. Samardzic-Boban, *Journal of Applied Crystallography*, **46**, 1670 (2013).
12. B. Ingham, M. Ko, N. Laycock, J. Burnell, P. Kappen, J. A. Kimpton and D. E. Williams, *Corrosion Science*, **56**, 96 (2012).
13. H. Wallander and J. Wallentin, *Journal of Synchrotron Radiation*, **24**, 925 (2017).
14. A. Atkinson and A. Marshall, *Corrosion Science*, **18**, 427 (1978).
15. G. M. Atenas, E. Mielczarski and J. A. Mielczarski, *J. Colloid Interface Sci.*, **289**, 157 (2005).
16. N. Paul, E. Metwalli, Y. Yao, M. Schwartzkopf, S. Yu, S. V. Roth, P. Muller-Buschbaum and A. Paul, *Nanoscale*, **7**, 9703 (2015).
17. R. Lazzari, F. Leroy and G. Renaud, *Physical Review B*, **76**, 125411 (2007).
18. A. Gibaud, S. Dourdain and G. Vignaud, *Applied Surface Science*, **253**, 3 (2006).
19. Y. P. Feng, S. K. Sinha, C. A. Melendres and D. D. Lee, *Physica B*, **221**, 251 (1996).
20. B. Lee, C.-T. Lo, P. Thiyagarajan, D. R. Lee, Z. Niu and Q. Wang, *Journal of Applied Crystallography*, **41**, 134 (2008).
21. C. A. Melendres, Y. P. Feng, D. D. Lee and S. K. Sinha, *Journal of the Electrochemical Society*, **142**, L19 (1995).
22. G. J. Ward, in *Siggraph 92 : Conference Proceedings*, S. Cunningham Editor, p. 265, Computer Graphics (1992).
23. B. Ingham, *Journal of Applied Crystallography*, **47**, 166 (2014).
24. M. Ko, B. Ingham, N. Laycock and D. E. Williams, *Corrosion Science*, **90**, 192 (2015).
25. A. Schreiber, C. Rosenkranz and M. M. Lohrengel, *Electrochimica Acta*, **52**, 7738 (2007).
26. C. C. Streinz, J. W. Wagner, J. Kruger and P. J. Moran, *Journal of the Electrochemical Society*, **139**, 711 (1992).
27. Y. Takabatake, K. Fushimi, T. Nakanishi and Y. Hasegawa, *Journal of the Electrochemical Society*, **161**, C594 (2014).
28. Y. Takabatake, Y. Kitagawa, T. Nakanishi, Y. Hasegawa and K. Fushimi, *Journal of the Electrochemical Society*, **164**, C349 (2017).
29. M. T. Woldemedhin, D. Raabe and A. W. Hassel, *Physica Status Solidi a-Applications and Materials Science*, **208**, 1246 (2011).
30. V. Maurice and P. Marcus, *Progress in Materials Science*, **95**, 132 (2018).
31. M. Ko, N. J. Laycock, B. Ingham and D. E. Williams, *Corrosion*, **68**, 1085 (2012).
32. M. H. Sk, A. M. Abdullah, M. Ko, N. Laycock, B. Ingham, M. P. Ryan and D. E. Williams, *ECS Transactions*, **80**, 509 (2017).
33. M. H. SK, A. M. Abdullah, M. Ko, N. Laycock, B. Ingham and D. E. Williams, *ECS Transactions*, **75**, 17 (2017).
34. J. Schultze, M. Lohrengel and D. Ross, *Electrochimica Acta*, **28**, 973 (1983).

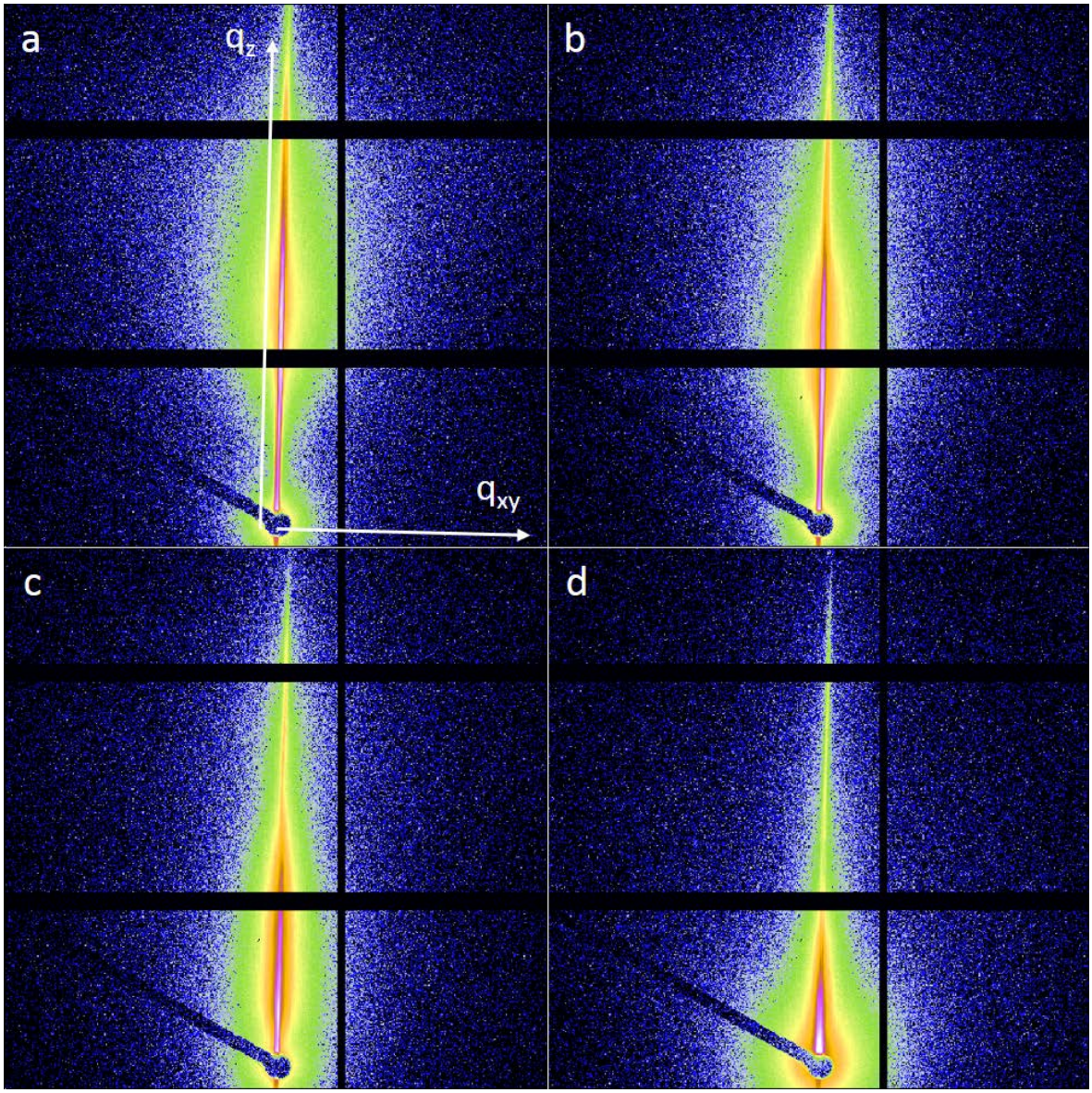

Figure 1. Selected raw GISAXS images from an experiment where a mild steel electrode was corroded electrochemically at o.c.p. + 200 mV in a 0.5 M NaCl, CO_2-saturated solution with pH = 6.8 at 80°C, at times from application of current: (a) 0 s, (b) 18 s, (c) 110 s, (d) 600 s (o.c.p denotes open circuit potential). The q_{xy} and q_z directions are indicated in (a). The horizontal and vertical black bars are gaps between the detector modules, while the diagonal bar is the beam stop.

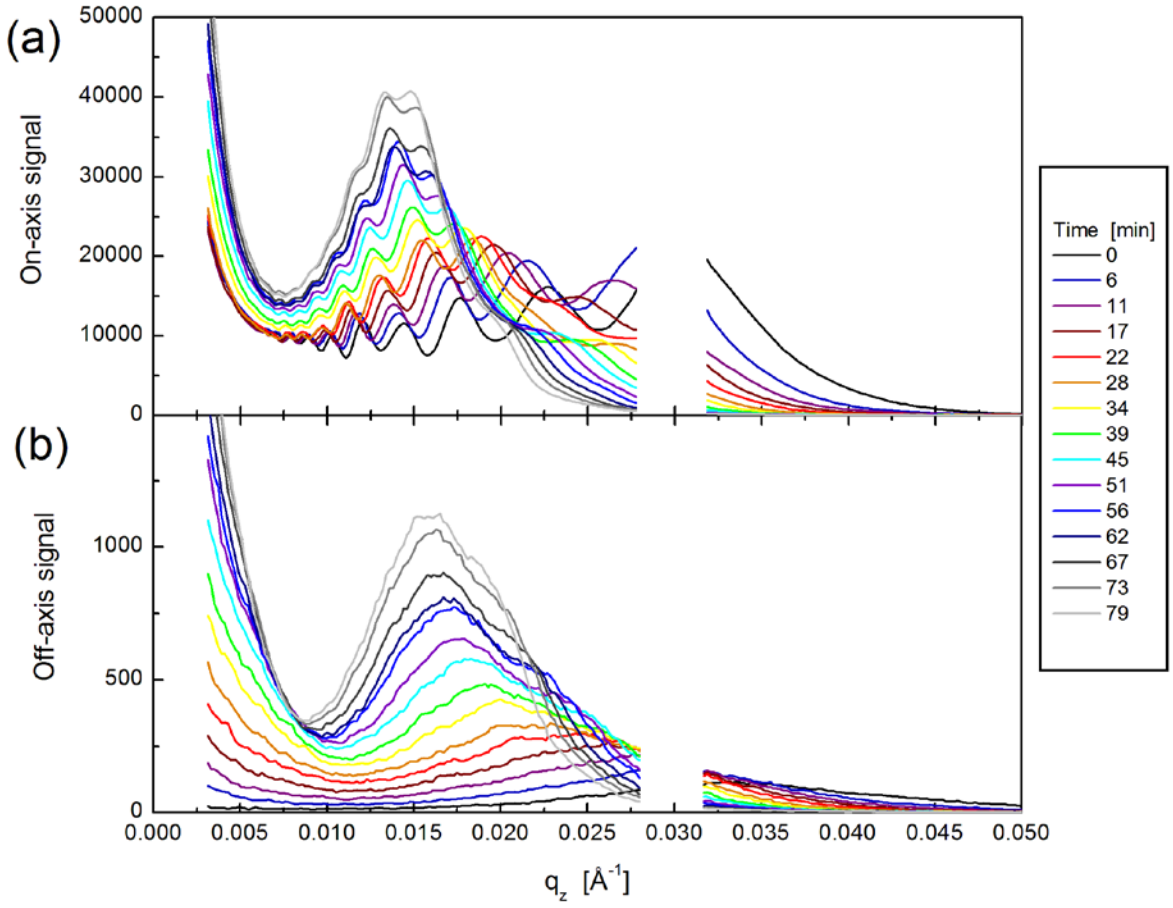

Figure 2. GISAXS intensity versus q_z,for mild steel corroding at the o.c.p. (-720 mV vs. Ag/AgCl) in a 0.5 M NaCl, CO_2-saturated solution with pH = 6.8 at 80°C. Two cuts at constant q_{xy} for a selection of scans is shown: (a) the specular (on-axis) scattering at q_{xy} = 0 Å^{-1} and (b) the diffuse (off-axis) scattering at q_{xy} = 0.002 Å^{-1}.

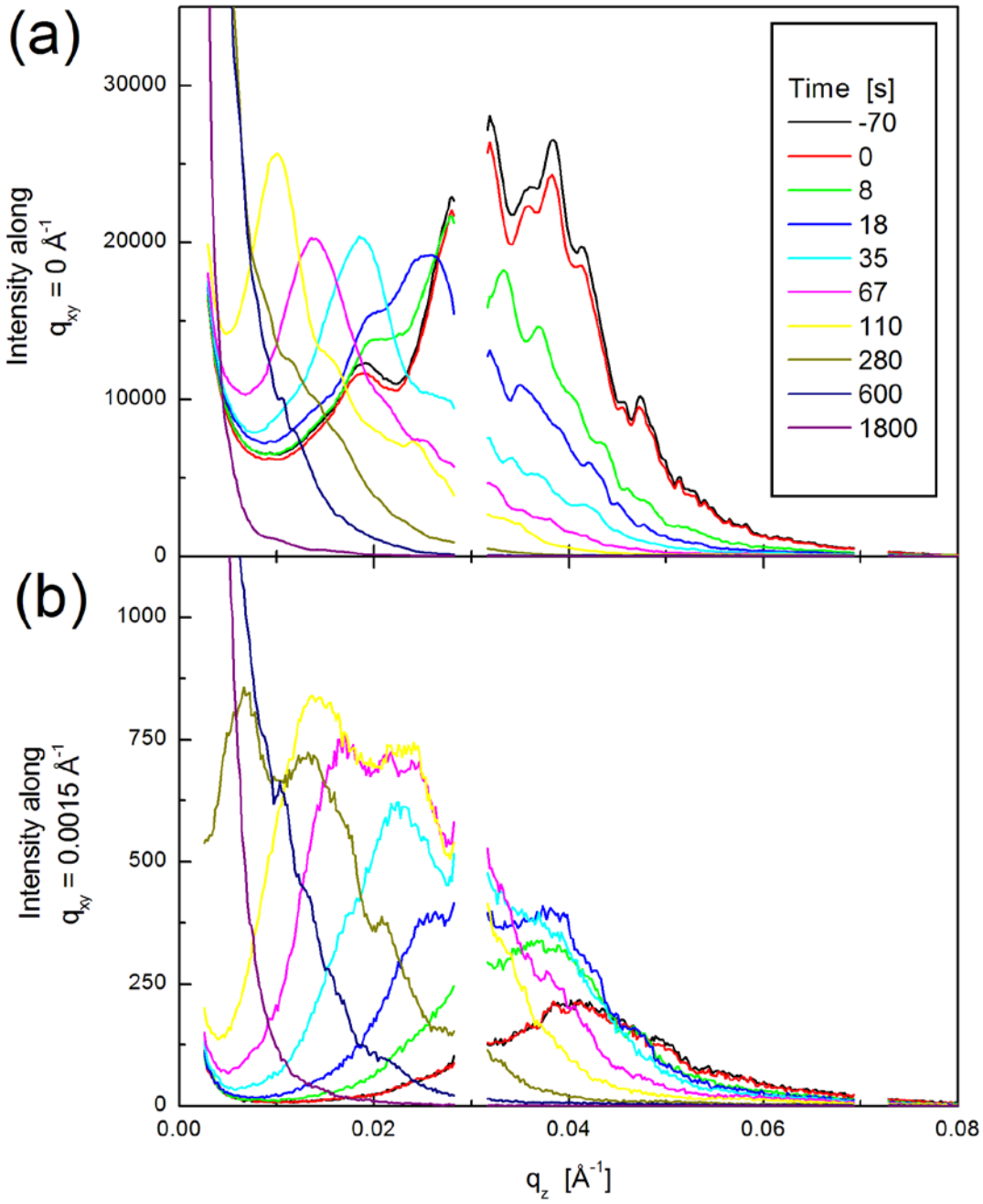

Figure 3. GISAXS intensity versus q_z, extracted from (a) the specular scattering, q_{xy} = 0 Å^{-1}, and (b) the diffuse scattering, q_{xy} = 0.0015 Å^{-1}, for selected scans from the experiment shown in Figure 1, at times as indicated.

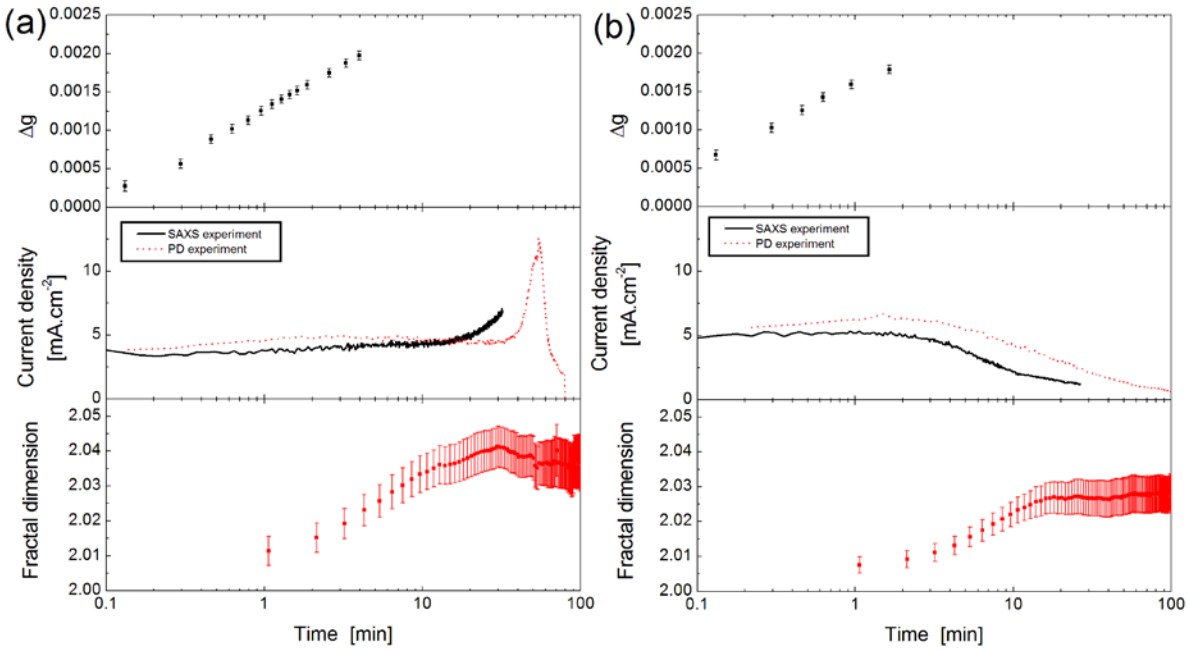

408

409

410 Figure 4. Variation with time of average surface gradient (for data where the specular peak
411 could be resolved), current density and fractal dimension, for (a) AISI 1006 mild steel and (b)
412 API 5CT L80 1Cr0.25Mo pipeline steel under anodic polarisation in CO_2-saturated 0.5M NaCl
413 at 80°C. The results are from separate synchrotron experiments carried out several months
414 apart.

415

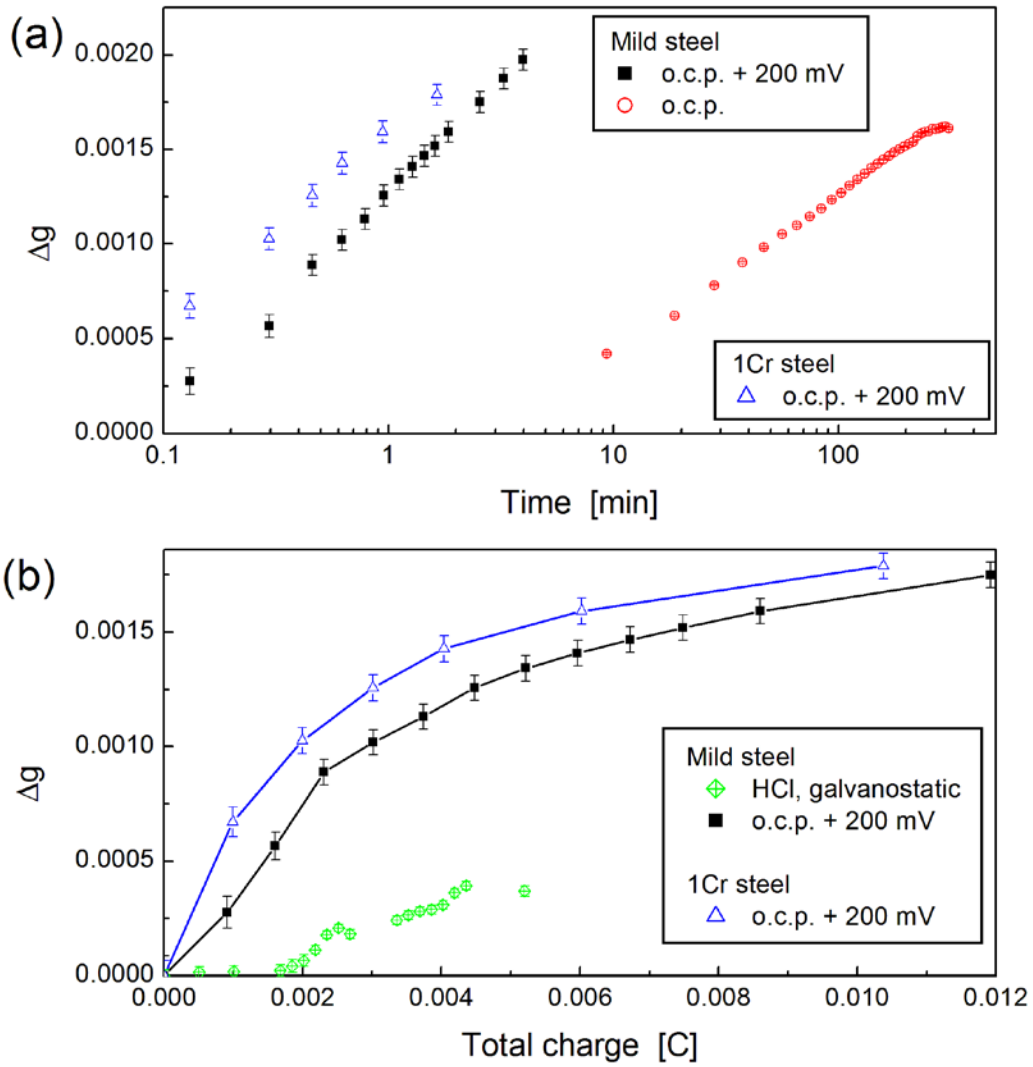

416

417 Figure 5. (a) Variation with time of average surface gradient, for AISI 1006 mild steel and API
418 5CT L80 1Cr0.25Mo pipeline steel, at the open circuit corrosion potential and under anodic
419 polarisation in CO_2-saturated 0.5M NaCl at 80°C. (b) Variation with total anodic charge
420 passed of average surface gradient, for AISI 1006 mild steel and API 5CT L80 1Cr0.25Mo
421 pipeline steel, under potentiostatic anodic polarisation in CO_2-saturated 0.5M NaCl at 80°C
422 and for AISI 1006 mild steel under galvanostatic polarisation at similar current density in
423 0.03 M HCl + 0.5 M NaCl electrolyte at room temperature.

424